Numerical modelling of gas–solid fluidized beds using the two-fluid approach

C. C. Pain*,1, S. Mansoorzadeh, C. R. E. de Oliveira and A. J. H Goddard

Computational Physics and Geophysics Group, T. H. Huxley School of Environment, Earth Sciences and Engineering, Imperial College of Science, Technology and Medicine, London, U.K.

SUMMARY

This paper details an approach to modelling gas–solid fluidized beds using the two-fluid granular temperature model. Details concerning the difficulties associated with the boundary conditions, particularly for curved boundaries, are described along with a novel means of obtaining the internal stress of the solid-phase, in part, by solving an implicit equation. This results in a scheme that is stable even when the solid volume fraction is close to maximum packing. A transient, mixed finite element discretization is used to solve the multi-phase equations with a discontinuous finite element representation of the granular temperature and continuity equations. A new solution method is proposed to solve the coupled momentum and continuity equations based on Arnoldi iteration. Two fluidized beds are modelled, one in the bubbling regime and the other in the slugging regime. These simulations are compared with experiments. Copyright © 2001 John Wiley & Sons, Ltd.

KEY WORDS: granular temperature; finite elements; fluidization; fluidized bed; multi-phase flow; numerical simulation; two-fluid model

1. INTRODUCTION

Fluidization is observed when a bed of solid particles comes into contact with a vertical upward fluid flow within a particular range of flow velocity [1]. Fluidized beds have many industrial applications, which can be classified according to their physical or chemical processes. Some examples of applications include solid drying, food freezing, granulation, dust/particle filtration, coating of pharmaceutical tablets, etc. Fluidized beds in the chemical industry include those in which the solid acts as catalyst or heat sink, such as in oil cracking for manufacturing of various chemical substances, and those in which solids undergo a phase change, such as in coal combustion, coal gasification, etc. Fluidized beds are used in industry

---

* Correspondence to: T.H. Huxley School of Environment, Earth Sciences and Engineering, Imperial College of Science, Technology and Medicine, Prince Consort Road, London, SW7 2BP, U.K.
1 E-mail: c.pain@ic.ac.uk

because of their large area of contact between the different phases, which enhances chemical reactions, heat transfer [2], mass transfer [3], etc. The predictive ability of numerical modelling appears to be a promising means of improving the efficiency of these beds and their processes.

Modelling the gas fluidization of particles and associated dynamics is a complex and challenging problem. Numerical approaches used include modelling the individual collisions (tracking individual particles) between particles subjected to the drag forces exerted by the fluidizing gases [4,5]. There are two models used to deal with interparticle collisions: the hard sphere model and the soft sphere model [6,7]. In these models, the impulse equations together with the restitution coefficient relate the velocities of particles before and after the collision. In the soft sphere model, the forces acting on the particle during contact are also considered. This is perhaps the most fundamental viable modelling approach. It explicitly models granular turbulence, but is computationally expensive when the particles are closely packed as in a typical fluidized bed. A model of individual particles' motions along with the flow around these has been developed for the two-dimensional case in Reference [8] using a moving finite element and adaptive meshing method. Some of the general properties of particles' motions were observed in the resulting simulations, such as a tendency for particles to collect together.

A scattering kernel for each fluid element could be calculated based on probabilities that depend on the angular and speed distribution of particles within the fluid element. This kernel can be used to construct the associated Boltzmann equation, which could be solved deterministically in the full phase space (space, angle, speed, time) (see Reference [9]). The programming complexity and envisaged large computational demands have not made this approach popular.

At the other modelling extreme are the two-fluid models (TFM) [10,11], whose initial development was based on the observation that closely packed fluidized particles have dynamics similar to a low-Reynolds number fluid flow. They thus assume a continuum description of the fluidized system. Among the first models to be developed were those based on the analogy with porous media with the use of Darcy Law assumptions [12] (neglecting inertial terms).

Useful predictions have been made using a two-fluid model with a momentum equation set for each of the gas- and solid-phases. However, these have often been plagued by uncertainties in prescribing the isotropic viscosity and normal stress of the solids phase. Various non-Newtonian models for the internal stresses of the solid-phase have been proposed [11,13]. These stresses were correlated with experimental observations. The resulting uncertainties have led to the increase in the popularity of the granular temperature model, which is based on an analogy between the kinetic theory of gases and binary particle–particle collisions [14–19]. This provides a means of calculating the internal stresses for the solid-phase without resorting to correlations. Works performed in References [20–22] have shown the ability of the two-fluid granular temperature approach to model numerically the bubbling gas–solid fluidized bed.

The history of the modelling of fluidized beds can be found in Reference [23], details of the turbulent modelling can be found in References [16,20,22] and the general behaviour of fluidized beds, including various correlations, can be found in References [3,24,25].

Other important numerical modelling works include Reference [20], in which coupled turbulent models for both the solid- and gas-phases were used. Kuipers *et al.* [2] investigated numerical heat transport within a fluidized bed and, in Reference [21], predicted (from the granular temperature TFM) velocity fluctuations of particles were compared with experimental fluctuations, with varying restitution coefficients.

A large number of codes have the ability to model multi-phase flows (although they may not be written for solid–gas flows), for example, PHOENICS [26], which uses the SIMPLE based interphase slip algorithm (ISPN). These types of algorithms seem, to date, to be the most successful and robust multi-phase solutions. Some other multi-phase codes are CFX, FLU-ENT, RELAP5 [27], TRAC [28] and CATHARE [29]. The latter seems rather different from the others, which are project-based algorithms with Pickard iteration. CATHARE uses direct, frontal solutions of the coupled main variables and Newton iteration.

In this paper we attempt to model gas–solid particle fluidized beds using the two-phase solution method, assuming both gas- and solid-phases are incompressible. The pressure differences in the gas-phase are small enough for this assumption to be valid for the examples presented. A transient mixed finite element formulation is used to discretize the equations. In addition, a discontinuous finite element (finite volume) discretization of the continuity equations and field variables and a continuous Petrov–Galerkin [30] discretization of the momentum equations are employed. Within each time step the equations are iterated upon using a projection-based pressure determination method until all equations balance simultaneously. As a result, the non-linear continuity equations are strictly satisfied, ensuring mass conservation.

The remainder of the paper is structured as follows: Section 2 presents the governing equations along with appropriate boundary conditions; Section 3 contains a description of the discretization and solution method used to solve these equations; Section 4 presents the numerical results; and conclusions are drawn in Section 5.

2. GOVERNING EQUATIONS AND ASSOCIATED BOUNDARY CONDITIONS

In this section we present the governing equations for the two-fluid numerical model solved here, along with the associated boundary conditions. Detailed derivation of these equations can be found in Reference [22] and the boundary conditions in Reference [31]. In the examples presented and in the numerical description, both phases are assumed incompressible, which is a reasonable approximation of the adiabatic flows considered in the applications (Section 4).

2.1. Governing equations

The continuity equations for phase k, where $k = \mathrm{g}$ denotes gas and $k = \mathrm{s}$ denotes solid particles, is

$$\frac{\partial}{\partial t}(\alpha_k \rho_k) + \frac{\partial}{\partial x_i}(\alpha_k \rho_k v_{k_i}) = 0 \tag{1}$$

where ρ_k is the density of phase k, α_k is the volume fraction of phase k, v_k the velocity of phase k, t is time and x_i is the spatial co-ordinate in the ith direction. The corresponding momentum equation is

$$\frac{\partial}{\partial t}(\alpha_k \rho_k v_{k_i}) + \frac{\partial}{\partial x_j}(\alpha_k \rho_k v_{k_i} v_{k_j}) = -\alpha_k \frac{\partial p_\mathrm{g}}{\partial x_i} + \alpha_k \rho_k g_i + \beta(v_{k'_i} - v_{k_i}) + \frac{\partial}{\partial x_i}(\tau_{k_{ij}}) \tag{2}$$

where g_i is the component of gravity in the ith direction, k' denotes the opposite phase, p_g is the shared pressure and β is the friction coefficient.

In this equation, τ is the stress, which for the gas-phase g is

$$\tau_{g_{ij}} = 2\alpha_g \mu_g S_{g_{ij}} \tag{3}$$

where

$$S_{g_{ij}} = \frac{1}{2}\left(\frac{\partial v_{g_i}}{\partial x_j} + \frac{\partial v_{g_j}}{\partial x_i}\right) - \frac{1}{3}\frac{\partial v_{g_k}}{\partial x_k} \tag{4}$$

Here, gas-phase turbulence has been neglected because of the considerable uncertainties in turbulence model closures and the large gas-phase turbulent suppression [22] in the densely packed beds considered here. Instead, a constant viscosity is used which equals the gas viscosity in this case but could also be made larger to act as an eddy viscosity. In the solid phase, the stress is given by

$$\tau_{s_{ij}} = \left(-p_s + \alpha_s \zeta_s \frac{\partial v_{s_k}}{\partial x_k}\right)\delta_{ij} + 2\alpha_s \mu_s S_{s_{ij}} \tag{5}$$

where p_s is the solid-phase pressure given by

$$p_s = \alpha_s \rho_s [1 + 2(1+e)\alpha_s g_0]T + \hat{p}_a \tag{6}$$

T is the granular temperature (associated with kinetic energy of particle motion) and is defined by $\frac{3}{2}T = \frac{1}{2}C^2$, where $\overline{C^2}$ is the mean square velocity deviation from the average velocity v_s of the solid phase. Equation (6) has been altered from that presented in Reference [22] to include the term $\hat{p}_a$, which will be defined later. The solid-phase deformation rate is given by

$$S_{s_{ij}} = \frac{1}{2}\left(\frac{\partial v_{s_i}}{\partial x_j} + \frac{\partial v_{s_j}}{\partial x_i}\right) - \frac{1}{3}\frac{\partial v_{s_k}}{\partial x_k} \tag{7}$$

The solid shear viscosity μ_s is given by

$$\mu_s = \frac{4}{5}\alpha_s \rho_s d_s g_0 (1+e)\left(\frac{T}{\pi}\right)^{1/2} \tag{8}$$

where d_s is the diameter of the particles and e is the particle–particle restitution coefficient. In this equation for μ_s, and similarly for the equation used to calculate granular conductivity κ, we have included only the collisional interaction between particles and have ignored the kinetic contribution, which is relatively small for the densely packed beds considered here. The kinetic part is dominant for flows with small particle volume fractions and was included in the formulation of Reference [21].

The solid-phase bulk viscosity is

$$\zeta_s = \frac{4}{3}\,\alpha_s\rho_s d_s g_0(1+e)\left(\frac{T}{\pi}\right)^{1/2} \tag{9}$$

Various correlations are reported in the literature for the radial distribution function g_0 [17,22,32,33]. Here we use a correlation based on Reference [17] but amended to produce an improved fit to the results presented in Reference [33]

$$g_0 = \frac{3}{5}\left[1-\left(\frac{\alpha_s}{\alpha_*}\right)^{1/3}\right]^{-1} \tag{10}$$

where α_* is the particle volume fraction at maximum packing.

The friction coefficient β is

$$\beta = \begin{cases} 150\dfrac{(\alpha_s)^2\mu_g}{\alpha_g d_s^2} + 1.75\dfrac{\rho_g\alpha_s|v_g-v_s|}{d_s}, & \text{for } \alpha_s \leq 0.8 \\[2mm] \dfrac{3}{4}\,C_d\,\dfrac{\alpha_g\alpha_s\rho_g|v_g-v_s|}{d_s}\,\alpha_g^{-2.65}, & \text{otherwise} \end{cases} \tag{11}$$

where for

$$Re_p = \frac{\alpha_s\rho_g|v_g-v_s|d_s}{\mu_g} < 1000$$

the drag coefficient is

$$C_d = \frac{24}{Re_p}[1 + 0.15(Re_p)^{0.687}] \tag{12}$$

and for $Re_p > 1000$

$$C_d = 0.44$$

Here, Re_p is the particle Reynolds number.

The fluctuation energy equation is

$$\frac{3}{2}\left(\frac{\partial(\alpha_s\rho_s T)}{\partial t} + \frac{\partial}{\partial x_j}(\alpha_s\rho_s v_j T)\right) = \tau_{s_{ij}}\frac{\partial v_{s_i}}{\partial x_j} - \frac{\partial q_j}{\partial x_j} - \gamma - 3\beta T \tag{13}$$

The term $-3\beta T$ represents the loss of particle kinetic energy to the gas-phase due to particle–gas drag forces. The corresponding source term due to turbulent velocity fluctuations of the gas-phase has been ignored. This is a necessity in the absence of a gas-phase turbulence model and can be justified for heavy large particles [34].

The collisional energy dissipation γ is given by

$$\gamma = 3(1 - e^2)(\alpha_s)^2 \rho_s g_0 T \left[\frac{4}{d_s} \left(\frac{T}{\pi} \right)^{1/2} \frac{\partial v_k}{\partial x_k} \right] \tag{14}$$

and the flux of fluctuating energy by

$$q_j = -\kappa \frac{\partial T}{\partial x_j} \tag{15}$$

with a granular conductivity κ defined as

$$\kappa = 2\rho_s (\alpha_s)^2 g_0 d_s \left(\frac{T}{\pi} \right)^{1/2} \tag{16}$$

2.2. Boundary conditions

In order to solve the set of equations obtained for the gas-solids flow, appropriate boundary conditions for velocity and volume fraction of both phases and the granular temperatures of the solid-phase are necessary. The volume fraction of gas is set to unity where gas enters the system. The particles may slip at the wall or bounce off the wall, creating complicated boundary conditions that will require simplification for use with the TFM.

The boundary conditions for gas- and solid-phases at the walls are: (i) prescribed shear stress—obtained from the Blasius equation for gas (see Reference [35]) with a length scale equal to the height of the initial solid occupied domain (approximated with the shear stress of gas on a plane surface measured at a length equal to this height); (ii) no normal flow; (iii) prescribed fluctuating energy flux. At the top of the domain all components of the gas (air) stress tensor are set to zero, allowing the gases to enter and leave the domain unhindered. Since pressure is the dominant part of the total normal stress component, this in effect sets the shared pressure level to zero at the top most part of the domain (outlet boundary). Thus, the atmospheric pressure level must be added to this pressure, where pressure is needed for compressible flow. No normal flow and zero shear stress conditions are applied to the solid-phase at the top most boundary, so there is no loss of solid in the simulations.

The boundary conditions applied to the particle-phase can be summarized as follows. Defining R as [36]

$$R = \frac{7}{2} \left(\frac{1 + e}{1 + \beta_0} \right) \frac{S}{N}$$

where e is the wall restitution coefficient, β_0 is the tangential coefficient of restitution at the wall, N is the normal stress (the solid-phase pressure p_s is used here to approximate N) and S is the shear stress. The shear stress at the wall can be calculated from the following correlation:

$$R = \begin{cases} \dfrac{3}{2}r, & 1 \leq r \leq \dfrac{2}{3}\mu_0 \\[2ex] \mu_0, & \dfrac{2}{3}\mu_0 \leq r \leq \infty \end{cases}$$

where

$$r = \frac{v_{\text{wall}}}{(3T)^{0.5}}, \qquad \mu_0 = \frac{7}{2}\left(\frac{1+e}{1+\beta_0}\right)\mu$$

in which v_{wall} and T are the slip velocity and granular temperature of the particle near the wall respectively and μ is the friction coefficient.

The normalized frictional flux F is defined as

$$F = \frac{7}{2}\frac{1+e}{1+\beta_0}\left[\frac{Q}{N\sqrt{3T}} + \frac{3}{8}(1-e)\right]$$

In Reference [36] an expression for F was determined

$$F = \begin{cases} \dfrac{3}{8}[2(1+\beta_0)r^2 - (1-\beta_0)], & 1 \leq r^2 \leq \dfrac{1}{2}\left[\mu_0^2 + \dfrac{1-\beta_0}{1+\beta_0}\right] \\[3ex] \dfrac{3}{8}(1+\beta_0)\mu_0^2, & \dfrac{1}{2}\left[\mu_0^2 + \dfrac{1-\beta_0}{1+\beta_0}\right] \leq r^2 \leq \infty \end{cases}$$

where Q is the rate at which fluctuation energy is provided to the flow per unit area of the wall. This provides a convenient expression for $Q = q \cdot n$ (q is the flux of fluctuating energy, Equation (15), and n is the normal to the boundary), which is applied in a natural finite element sense [30].

3. NUMERICAL SOLUTION OF MULTI-PHASE FLOW EQUATIONS

The numerical solution of the equations above involves two steps: in what follows, the momentum and continuity equations are discretized using a mixed finite element formulation with a discontinuous representation of the volume fraction fields. Before the momentum equations are discretized they are first divided by the volume fraction of the corresponding phase. The resulting coupled equations are then solved using a projection-based method (Richardson iteration), which is adapted to the multi-phase case.

3.1. Finite element discretization

The momentum equations are discretized implicitly in time using the backward Euler method, with upwind discretization of the non-linear terms, the magnitude of which is chosen to obtain the 'correct' quantity of dissipation at steady state (see Reference [30] and Section 3.2.3). All

the resulting mass matrices are lumped to enhance convergence of the solvers. The difficulties associated with a multi-phase solution will be illustrated here in two-dimensional Cartesian co-ordinates. Suppose

$$\underline{v} = \begin{pmatrix} \underline{v}_g \\ \underline{v}_s \end{pmatrix}$$

with

$$\underline{v}_k = \begin{pmatrix} \underline{v}_{k_x} \\ \underline{v}_{k_y} \end{pmatrix} \quad \text{and} \quad \underline{p} = \begin{pmatrix} \underline{p}_g \\ \underline{p}_a \end{pmatrix}$$

the vectors of unknowns associated with velocity and pressure respectively. Suppose v_{k_x}, α_k and p_k have finite element expansions $v_{k_x} = \Sigma_j N_j v_{k_{x_j}}$, $\alpha_k = \Sigma_j M_j \alpha_{k_j}$ and $p_k = \Sigma_j M_j p_{k_j}$. Thus, the vectors $\underline{v}_{k_x}$, $\underline{\alpha}_k$ and $\underline{\alpha}_k$ contain

$$\underline{v}_{k_x} = \begin{bmatrix} v_{k_{x1}} \\ v_{k_{x2}} \\ v_{k_{x3}} \\ \vdots \end{bmatrix}, \qquad \underline{\alpha}_k = \begin{bmatrix} \alpha_{k1} \\ \alpha_{k2} \\ \alpha_3 \\ \vdots \end{bmatrix} \quad \text{and} \quad \underline{p}_g = \begin{bmatrix} p_{g1} \\ p_{g2} \\ p_{g3} \\ \vdots \end{bmatrix}$$

respectively. v_{k_x}, v_{k_y} are the x and y components of velocity of phase k respectively. An expansion similar to that of v_{k_x} is used for v_{k_y}. The coefficients of this expansion are placed in the vector of unknowns $\underline{v}_{k_y}$. The pressure $\underline{p}_a$ is associated with the solid-phase, but not necessarily the solid-phase pressure $\underline{p}_s$, Equation (6).

The granular temperature associated with the solid-phase is approximated with the series $T = \Sigma_j M_j T_j$. The simulations presented will employ an M_i that is piecewise constant (constant throughout an element) and an N_j that is the continuous bilinear finite element method (FEM) basis function—both sets of basis functions with local support. Thus, the role of i and j will change from here on, so instead of representing the component of velocity and dimension as they were used previously, they are now used to identify basis functions. A subscript k continues to indicate the phase, which may be replaced by a 'g' for the gas-phase or an 's' to denote the solid-phase. The time level at which the variables are evaluated is indicated from here on with a superscript, for example $\underline{\alpha}_k^n$ is the vector of volume fractions of phase k at time level n. Details of discretization using these basis functions for single phase flow can be found in Reference [37]. The momentum equation (2), discretized, becomes

$$A \frac{\underline{v}^{n+1}}{\Delta t} = C\underline{p}^{n+1} + \underline{S}^{n+1} \tag{17}$$

Matrix A contains implicit coupling terms between the phases as well as implicit discretization within each phase, and the vector $\underline{S}^{n+1}$, as well as terms involving $\underline{v}^n$, contains sources and sinks of momentum, e.g. body forces. Matrix C is defined, for example, as

$$C = \begin{pmatrix} C_g & 0 \\ C_g & C_a \end{pmatrix}, \quad \text{with} \quad C_g = \begin{pmatrix} C_{g_x} \\ C_{g_y} \end{pmatrix}$$

Matrix C_a will be defined in Section 3.1.2. The values at row i and column j of the matrices C_{g_x} and C_{g_y} are

$$C_{g_{x_{ij}}} = \int \frac{\partial N_i}{\partial x} M_j \, dV \quad \text{and} \quad C_{g_{y_{ij}}} = \int \frac{\partial N_i}{\partial y} M_j \, dV$$

respectively. The discretized continuity equations (1) are

$$M_\alpha \left(\frac{\underline{\alpha}_k^{n+1} - \underline{\alpha}_k^n}{\Delta t} \right) + \mathscr{C}_k^T(\alpha_k^{n+1}) \underline{v}_k^{n+1} = \underline{0} \tag{18}$$

with

$$\mathscr{C}_k(\alpha_k^n)_{ij} = \begin{bmatrix} \sum_e \left(\int_e \left(\alpha_k^n \frac{\partial N_i}{\partial x} + \frac{\partial \alpha_k^n}{\partial x} N_i \right) M_j \, dV - \int_{ev_{k_x} n_x < 0} N_i n_x^e M_j (\alpha^n - \alpha_{in}^n) \, d\Gamma \right) \\ \sum_e \left(\int_e \left(\alpha_k^n \frac{\partial N_i}{\partial y} + \frac{\partial \alpha_k^n}{\partial y} N_i \right) M_j \, dV - \int_{ev_{k_y} n_y < 0} N_i n_y^e M_j (\alpha^n - \alpha_{in}^n) \, d\Gamma \right) \end{bmatrix} \tag{19}$$

The mass matrix M_α has entries $M_{\alpha_{ij}} = \int M_i M_j \, dV$, e denotes the element, α_{in}^n represents the volume fraction from neighbouring elements, $\begin{pmatrix} n_x^e \\ n_y^e \end{pmatrix}$ is the normal to element e along boundary Γ of element e, and $\underline{0}$ represents the vector containing entries of zero only. Summing continuity Equation (18) over all phases, the overall continuity equation is obtained

$$\sum_k \mathscr{C}_k^T(\alpha_k^{n+1}) \underline{v}_k^{n+1} = \underline{0}$$

The terms

$$\frac{\partial \alpha_k^n}{\partial x}, \quad \frac{\partial \alpha_k^n}{\partial y}$$

in Equation (19) disappear for the constant variation of α_k^n throughout an element used here, but remain for higher-order variations of α_k^n within each element. A spatially higher-order

discretization method can also be realized by replacing α_{in}^n in Equation (19) by an interpolated value of α_k^{n+1}. This would need to be limited to avoid unphysical volume fractions resulting in a high-resolution method. Similarly, the time stepping given by Equation (18) can also be extended to a second-order, or higher, method in time.

The consistent manner in which $\nabla \cdot v_k \alpha_k$ is discretized in $\mathscr{C}_k$ of Equation (18) ensures that the overall scheme preserves the integral of α_k over the solution domain in the absence of phasic mass exchange and boundary conditions for α_k, i.e. inlet values of α_k.

3.1.1. Boundaries not aligned with the co-ordinate system. For curved wall boundaries $\alpha_{k_{in}} = 0$, $\forall k$ is the default boundary condition. This ensures that no net solid enters or leaves the domain at curved boundaries, or any boundaries for that matter, with no normal flow boundary conditions imposed. This is necessary because there may be an inlet or outlet velocity component normal to the elements on curved boundaries in which no normal flow boundary conditions are imposed.

In order to apply specified shear stress boundary conditions at curved boundaries (walls) or boundaries not aligned with the co-ordinate system, the co-ordinate system is rotated so that it is aligned with the boundary. No normal flow boundary conditions can be applied in the rotated system as a velocity component set to zero. For continuity satisfying reasons, see Reference [38], the normal to the boundaries (centred at node j say) are obtained from the matrices C_{g_x}, C_{g_y} (used to define the discretized continuity equations for single phase flow), via

$$n_j = (n_{x_j}, n_{y_j}) = \frac{1}{n^*}\left(\sum_i C_{g_{x_{ij}}}, \sum_i C_{g_{y_{ij}}}\right)$$

in which n^* normalizes the vector n_j. The local rotation matrix at boundary node j is

$$\mathscr{R}_j = \begin{pmatrix} -n_{y_j} & n_{x_j} \\ n_{x_j} & n_{y_j} \end{pmatrix}$$

Defining the diagonal matrices $\mathscr{D}_x$ and $\mathscr{D}_y$ to have entries $\mathscr{D}_{x_{ij}} = n_{x_j}\delta_{ij}$ and $\mathscr{D}_{y_{ij}} = n_{y_j}\delta_{ij}$ respectively, the rotation matrix for a single phase can be written as

$$R = \begin{pmatrix} -\mathscr{D}_y & \mathscr{D}_x \\ \mathscr{D}_x & \mathscr{D}_y \end{pmatrix}$$

The two-phase rotation matrix is, therefore

$$\hat{R} = \begin{pmatrix} R & 0 \\ 0 & R \end{pmatrix}$$

Matrices A, M and C are replaced by their rotated counterparts $A_r = \hat{R}A\hat{R}^T$, $M_r = \hat{R}M\hat{R}^T$ and $C_r = \hat{R}C$ respectively. All rotation matrices have the property that $R^T R = I$. This definition of C_r is also valid if the pressure vector $\underline{p}$ contains only the pressures associated with the gas $\underline{p}_g$.

The discretized momentum equation becomes

$$A_r \frac{\underline{v}_r^{n+1}}{\Delta t} = C_r \underline{p}^{n+1} + \underline{S}_r^{n+1}$$

with $\underline{v}_r = \hat{R}\underline{v}$ and $\underline{S}_r = \hat{R}\underline{S}$. The appropriate pressure equation can now be obtained by manipulating the relevant equations, as described in the next section, which includes the rotated continuity equation

$$M_\alpha \frac{\underline{\alpha}_k^{n+1} - \underline{\alpha}_k^{n+1}}{\Delta t} + \mathscr{C}_{k\ r}^T(\alpha_k^{n+1})\underline{v}_{k\ r}^{n+1} = \underline{0}$$

3.1.2. Solid-phase pressure. In References [2,11,13] the modulus of elasticity G was incorporated into the normal stress (solids added pressure) component with the application of the chain rule. That is

$$\frac{\partial p_s}{\partial y} = \frac{\partial p_s}{\partial \alpha_s} \frac{\partial \alpha_s}{\partial y}$$

with $G = \partial p_s / \partial \alpha_s$, which took on values correlated from experiments, in fact Reference [39] summarizes 15 different expressions, correlating solid pressure with bulk solid volume fraction.

In this section, the solid-phase pressure defined by Equation (6) will be used. It is important when the volume fraction of the solid-phase approaches its maximum to treat this pressure implicitly or partially implicitly because the acoustic wave speed of the solid-phase then approaches infinity (this phase becomes incompressible). An explicit pressure treatment is numerically unstable for incompressible flow. With an implicit treatment of solid-phase pressure, propagating solid-phase pressure waves need to be resolved to achieve numerical stability.

Suppose the equation for solid-phase pressure is

$$\alpha_s = L_s p_s \tag{21}$$

which is also the equation of state for the solid-phase, see References [32,33]. The function L_s used here is

$$L_s = \frac{1}{\rho_s(1 + 2(1 + e)\alpha_s g_0)T + \hat{p}_a/\alpha_s} \tag{22}$$

If Equation (21) is used in the discretized continuity equation (18), then the continuity equation (18) becomes

Copyright © 2001 John Wiley & Sons, Ltd.

Int. J. Numer. Meth. Fluids 2001; **36**: 91–124

$$\frac{1}{\Delta t} H_s^{n+1} \underline{p}_s^{n+1} + \mathscr{C}_s^T(\alpha_s^{n+1}) \underline{v}_s^{n+1} = \underline{h}_s^n \tag{23}$$

with the matrix H_s^n having components $H_{s_{ij}}^n = \int M_i L_s^n M_j \, \mathrm{d}V$, $\underline{h}_s^n = (1/\Delta t) H_s^n \underline{p}_s^n$ and the super-script n in L_s^n indicates that all components of L_s, given by Equation (22), are evaluated at time level n. Equation (23) is non-linear and thus an iteration level l must be introduced. Equation (23) then becomes

$$\frac{1}{\Delta t} H_{s\,l}^{n+1} \underline{p}_{s\,l}^{n+1} + \mathscr{C}_s^T(\alpha_{s\,l}^{n+1}) \underline{v}_{s\,l+1}^{n+1} = \underline{h}_s^n \tag{24}$$

The volume fractions can be calculated from

$$M_\alpha \frac{\underline{\alpha}_{s\,l+1}^{n+1} - \underline{\alpha}_s^n}{\Delta t} + \mathscr{C}_s^T(\alpha_{s\,l+1}^{n+1}) \underline{v}_{s\,l+1}^{n+1} = \underline{0} \tag{25}$$

to obtain the new volume fraction $\alpha_{s\,l+1}^{n+1}$ for iteration $l+1$. This is the implicit version that ensures the volume fractions lie within their physically permitted limits of [0, 1]. It also propagates the new α_s^{n+1} quickly across the mesh. However, explicit treatment of Equation (25) realized by replacing $\mathscr{C}_k^T(\alpha_{k\,l+1}^{n+1})$ with $\mathscr{C}_k^T(\alpha_{k\,l}^{n+1})$ in Equation (25) ensures that $\Sigma_k \, \alpha_{k\,l}^{n+1} = 1$ when Equation (25) is solved for both phases, because the global continuity equation $\Sigma_k \, \mathscr{C}_k^T(\alpha_{k\,l}^{n+1}) v_{k\,l+1}^{n+1} = 0$ is satisfied. For additional stability, Equation (25) is treated implicitly and solved using GMRES [40]. In any event, at convergence of the non-linear method the same continuity equation (25) is satisfied, so that the three conditions

$$\sum_k \alpha_k = 1, \qquad \int \alpha_k \, \mathrm{d}V = \text{constant}, \ \forall k, \qquad \alpha_k \in [0, 1], \ \forall k \tag{26}$$

are enforced.

The discretized version of the continuity equation is also non-linear in v_k, because v_k defines the incoming directions, to an element, used in the definition of $\mathscr{C}_k^T(\alpha_k^n)$ given by Equation (19). The latest available velocities are generally used to calculate the element incoming directions. However, we have found that stability is improved if the inlet boundaries for each element (associated with incoming fluid) are re-determined only when the volume fractions are updated.

Potential problems with the definition of L_s, Equation (22), as $T \to 0$, are avoided by introduction of $\hat{p}_a$, which depends on the volume fraction only. The term $\hat{p}_a$ in Equation (22) is used to keep the particles apart as the maximum packing is approached. The aim is to obtain a p_s that will take on a representative pressure resulting from the particles in the bed that are in continuous contact (contact other than binary collisions). In a collapsed fluidized bed with no fluidized gas pumping through it, p_s takes on the hydrostatic pressure resulting from the weight of particles (neglecting gas weight).

Suppose $\hat{p}_a$ can be represented by the *ad hoc* equation

$$\hat{p}_a = \rho_s \alpha_s^3 g_0' F$$

and thus $\hat{L}_a \hat{p}_a = \alpha_s$, with

$$\hat{L}_a = \frac{1}{\rho_s \alpha_s^2 g_0' F} \quad \text{and} \quad g_0' = \left(1 - \left(\frac{\alpha_s}{\alpha_*'}\right)^{1/3}\right)^{-1}$$

Others have introduced similar pressures usually based on a power law [41]. In our work F has been chosen based on dimensional arguments to be $F = F_0 g d$ for some numerically tuned F_0 (F_0 is of order 1, in fact $F_0 = 1$ is used). However, F_0 can be chosen to produce strictly real characteristics when the granular temperature is zero, see Reference [42] for example. Numerical experiments have demonstrated that there may be some benefit in choosing the maximum packing factor α_*' in g_0' of the equation for $\hat{p}_a$ to be slightly lower than α_* used in g_0, say by 2 per cent. For solid spheres with no gas drag forces, buoyancy and solid-phase pressure balances lead to the equation for volume fraction of the solid

$$\alpha_s = \alpha_*' \left(1 - \frac{d}{h} \alpha_s^2\right)^3$$

in which h is the depth below the collapsed bed surface and d is the diameter of the solid particles. Figure 1 shows the variation of the volume fraction with dimensionless depth h/d
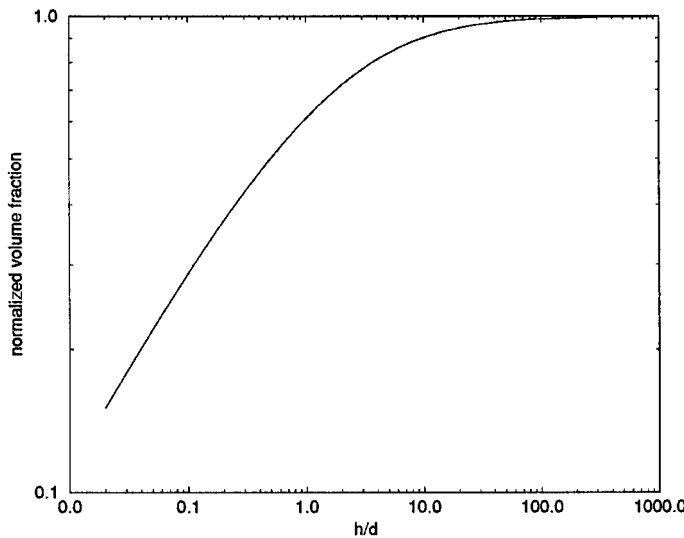

Figure 1. Normalized volume fraction of solid particles α_s/α_*' (with $\alpha_*' = 0.62$) against depth h below the collapsed bed surface divided by the diameter of the particles d.

below the surface. For numerical convenience, another parameter, p_a, is introduced and defined as

$$p_a = \frac{\alpha_s}{1 - \left(\dfrac{\alpha_s}{\alpha'_*}\right)^{1/3}}$$

with $\hat{p}_a = \rho_s F \alpha_s^2 p_a$. The pressure term $\nabla \hat{p}_a$ that appears on substituting p_s from Equation (21) into the solid-phase momentum equation (2) then becomes

$$\nabla \hat{p}_a = F(\alpha_s \nabla \alpha_s p_a \rho_s + \alpha_s p_a \rho_s \nabla \alpha_s)$$

On dividing this term by α_s, then discretizing, one obtains

$$\int N_i F(\nabla \alpha_s p_a \rho_s + p_a \rho_s \nabla \alpha_s)\, \mathrm{d}V = \int \left(-(\nabla N_i) F \alpha_s \rho_s p_a + N_i F(\nabla \alpha_s)\rho_s p_a \right) \mathrm{d}V + \int n N_i F \alpha_s \rho_s p_a\, \mathrm{d}\Gamma$$

$$= C_a p_a \tag{27}$$

This equation acts as a definition of the matrix C_a. To obtain the gradients $\partial \alpha_s/\partial x$, etc., in this equation, first values of the solid volume fraction at the nodes are calculated using an element average of α_s. This is then used with the weighting functions N_j, $\forall$ nodes j, to obtain the gradients. The boundary condition $\partial p_a/\partial n = 0$ is applied by feeding the volume-derived value of p_a into the surface integral above.

The term p_a which has been added to the solid-phase pressure p_s can be treated quite differently in the numerical scheme from the temperature-dependent term. In this work an implicit equation for the pressure term p_a is solved.

Now

$$\alpha_s = \left(1 - \left(\frac{\alpha_s}{\alpha'_*}\right)^{1/3}\right) p_a = L_a p_a$$

and this definition of $L_a = (1 - (\alpha_s/\alpha'_*)^{1/3})$ is used to obtain H_a in the continuity equation (24), which becomes

$$\frac{1}{\Delta t} H_{a\,l}^{n+1} \underline{p}_{a\,l}^{n+1} + \mathscr{C}_s^T(\alpha_{s\,l}^{n+1}) \underline{v}_{s\,l+1}^{n+1} = \underline{h}_a^n \tag{28}$$

with the matrix H_a^n having components $H_{a_{ij}}^n = \int M_i L_a^n M_j\, \mathrm{d}V$ and $\underline{h}_a^n = (1/\Delta t)H_a^n \underline{p}_a^n$. Using an analogy with density of single-phase fluid and $\alpha_s = \alpha_s(p_s, T)$, the speed of sound c_s in the solid-phase can be calculated using the chain rule

$$\frac{\partial \alpha_s}{\partial t} = \frac{\partial \alpha_s}{\partial p_s}\frac{\partial p_s}{\partial t} + \frac{\partial \alpha_s}{\partial T}\frac{\partial T}{\partial t}$$

with

$$\frac{1}{c_s^2} = \rho_s \frac{\partial \alpha_s}{\partial p_s}$$

and so differentiating Equation (21)

$$c_s^2 = T\left[1 + \frac{3}{5}\frac{(1+e)}{w(\alpha_s|\alpha_*)}\left(2\alpha_s w(\alpha_s|\alpha_*) + \frac{\alpha_s^2}{3\alpha_*\left(\frac{\alpha_s}{\alpha_*}\right)^{2/3}}\right)\right]$$

$$+ \frac{d_s g}{w(\alpha_s|\alpha'_*)^2}\left(3\alpha_s^2 w(\alpha_s|\alpha'_*) + \frac{\alpha_s^3}{3\alpha_*\left(\frac{\alpha_s}{\alpha_*}\right)^{2/3}}\right)$$

with

$$w(\alpha_s|\alpha'_*) = 1 - \left(\frac{\alpha_s}{\alpha'_*}\right)^{1/3}$$

It can be seen from this equation that as the volume fraction of the solid-phase approaches its maximum (α'_* or α_*), the acoustic wave speed c_s of the solid-phase approaches infinity.

When solving for the pressure p_a implicitly, the unknowns associated with p_a gathered together in the vector $\underline{p}_a$ must appear as part of the solution vector in the matrix equation and thus the vector of pressures $\underline{p}$ becomes

$$\underline{p} = \begin{pmatrix} \underline{p}_g \\ \underline{p}_a \end{pmatrix}$$

3.2. Resolution of the multi-phase equations

We employ a projection-based solution method to solve the discretized coupled equations. The general form of the method is presented next, followed by its extension to the case of multi-phase flows.

3.2.1. The projection method. Suppose that the discretized momentum and continuity equations are

$$\begin{bmatrix} \frac{1}{\Delta t}A & -C \\ -\mathscr{C}^T & -\frac{1}{\Delta t}H \end{bmatrix}\begin{pmatrix} \underline{v}^{n+1} \\ \underline{p}^{n+1} \end{pmatrix} = \begin{pmatrix} \underline{S}^{n+1} \\ \underline{h}^{n+1} \end{pmatrix}$$

A velocity field can be found that satisfies the discretized continuity equation exactly during any stage of an iterative process. Alternatively, if an implicit uncoupled non-iterative method is used to solve the discretized momentum equations, the resulting velocity field $\underline{v}_*^{n+1}$ will need some amendment in order to satisfy the discretized continuity equation exactly.

Suppose the discretized momentum equations that were solved to obtain $\underline{v}_*^{n+1}$ are

$$M \frac{\underline{v}_*^{n+1}}{\Delta t} = C \underline{p}_*^{n+1} + \underline{S}^{n+1} \tag{29}$$

This has a pressure field p_*^{n+1} that might not ensure continuity satisfaction. The pressure $\underline{p}^{n+1}$ and velocity $\underline{v}^{n+1}$ satisfy both the momentum equations

$$M \frac{\underline{v}^{n+1}}{\Delta t} = C \underline{p}^{n+1} + \underline{S}^{n+1} \tag{30}$$

and the continuity equations

$$\frac{1}{\Delta t} H \underline{p}^{n+1} + \mathscr{C}^T \underline{v}^{n+1} = \underline{h}^{n+1} \tag{31}$$

where

$$\underline{h}^{n+1} = \frac{1}{\Delta t} H \underline{p}^n$$

It is computationally convenient to solve for pressure correction. A pressure correction equation can be obtained by first subtracting Equation (29) from Equation (30) to obtain

$$M \left(\frac{\underline{v}^{n+1} - \underline{v}_*^{n+1}}{\Delta t} \right) = C \underline{\Delta p} \tag{32}$$

where $\underline{\Delta p} = \underline{p}^{n+1} - \underline{p}_*^{n+1}$.

Equation (32) is a spatial discretization version of

$$\frac{v^{n+1} - v_*^{n+1}}{\Delta t} = -\nabla \Delta p$$

Thus it is apparent that $\nabla \times v^{n+1} = \nabla \times v_*^{n+1}$, i.e. vorticity is unchanged.

Now, pre-multiplying Equation (32) by $\mathscr{C}^T M^{-1}$ and using Equation (31), the familiar pressure correction equation is obtained

$$\frac{-\dfrac{1}{\Delta t} H \underline{p}_*^{n+1} + \underline{h}^{n+1} - \mathscr{C}^T \underline{v}_*^{n+1}}{\Delta t} = \left(\mathscr{C}^T M^{-1} C + \frac{1}{\Delta t^2} H \right) \underline{\Delta p} \tag{33}$$

This equation is solved for $\underline{\Delta p}$, which is then placed into Equation (32) to obtain $\underline{v}^{n+1}$ via

$$\underline{v}^{n+1} = \underline{v}_*^{n+1} + \Delta t M^{-1} C \underline{\Delta p} \tag{34}$$

The resulting $\underline{v}^{n+1}$ by construction satisfies the discretized continuity equation (31), independent of the discretization of the momentum equations. In a practical application of the projection method, the momentum equation can be treated implicitly with a guessed value of pressure from the previous iteration, that is

$$A \frac{\underline{v}_*^{n+1}}{\Delta t} = C \underline{p}_*^{n+1} + \underline{S}^{n+1} \tag{35}$$

Continuity correcting algorithms such as this can be incorporated into iterative algorithms, such as those presented. An example of its usefulness is illustrated by the popular SIMPLER algorithm, which uses the method at the end of each iteration cycle [55].

3.2.2. Multi-phase solution method. In this subsection a pressure matrix will be obtained by the same procedure that was used to obtain Equation (33). However, the pressure matrix for the FEM is not symmetric-positive-definite, except in the one-dimensional case, with phase coupling treated explicitly in pressure, in which case it is equivalent to the donor cell approach. A symmetric-positive-definite matrix equation is solved in order to help obtain a solution to the discretized momentum equation (17) and continuity equations (18). These equations combined in matrix form are presented in Equation (36) below. The approximation is obtained with the aid of a second conservative discretization of this equation (see next subsection). The discretized momentum and continuity equations are

$$\begin{bmatrix} \dfrac{1}{\Delta t} A & -C \\ -\mathscr{C}^T & -\dfrac{1}{\Delta t} H \end{bmatrix} \begin{pmatrix} \underline{v} \\ \underline{p} \end{pmatrix} = \begin{bmatrix} \dfrac{1}{\Delta t} A_{gg} & \dfrac{1}{\Delta t} A_{gs} & -C_g & 0 \\ \dfrac{1}{\Delta t} A_{sg} & \dfrac{1}{\Delta t} A_{ss} & -C_g & -C_a \\ -\mathscr{C}_g^T & -\mathscr{C}_s^T & 0 & 0 \\ 0 & -\mathscr{C}_s^T & 0 & -\dfrac{1}{\Delta t} H_a \end{bmatrix} \begin{pmatrix} \underline{v}_g \\ \underline{v}_s \\ \underline{p}_g \\ \underline{p}_a \end{pmatrix} = \begin{pmatrix} \underline{s}_g \\ \underline{s}_s \\ \underline{h}_g \\ \underline{h}_a \end{pmatrix} \tag{36}$$

Its approximation double is

$$
\begin{bmatrix} \dfrac{1}{\Delta t} M & -C \\[2ex] -\mathscr{C}^T & -\dfrac{1}{\Delta t} H \end{bmatrix} \begin{pmatrix} \underline{v} \\[1ex] \underline{p} \end{pmatrix} = \begin{bmatrix} \dfrac{1}{\Delta t} M_{\mathrm{gg}} & \dfrac{1}{\Delta t} M_{\mathrm{gs}} & -C_{\mathrm{g}} & 0 \\[2ex] \dfrac{1}{\Delta t} M_{\mathrm{sg}} & \dfrac{1}{\Delta t} M_{\mathrm{ss}} & -C_{\mathrm{g}} & -C_a \\[2ex] -\mathscr{C}_{\mathrm{g}}^T & -\mathscr{C}_{\mathrm{s}}^T & 0 & 0 \\[2ex] 0 & -\mathscr{C}_{\mathrm{s}}^T & 0 & -\dfrac{1}{\Delta t} H_a \end{bmatrix} \begin{pmatrix} \underline{v}_{\mathrm{g}} \\[1ex] \underline{v}_{\mathrm{s}} \\[1ex] \underline{p}_{\mathrm{g}} \\[1ex] \underline{p}_a \end{pmatrix} = \begin{pmatrix} \underline{s}_{\mathrm{g}} \\[1ex] \underline{s}_{\mathrm{s}} \\[1ex] \underline{h}_{\mathrm{g}} \\[1ex] \underline{h}_a \end{pmatrix} \tag{37}
$$

where C_{s} is defined by Equation (27), M_{mn} is an approximation to the matrix A_{mn}. This is a particularly good approximation when the mass matrices contained within A_{mn} are all lumped, which they are in the examples presented. M_{mn} contains all the mass matrices in A_{mn}, lumped so that it is block diagonal, so in two dimensions M_{mn} contains two non-zeros per row and in three dimensions, three non-zeros per row. Matrix M contains all the coupling terms between the phases and thus these terms are treated fully implicitly.

The inverse of

$$
M = \begin{pmatrix} M_{\mathrm{gg}} & M_{\mathrm{gs}} \\ M_{\mathrm{sg}} & M_{\mathrm{ss}} \end{pmatrix}
$$

i.e. $D = M^{-1}$, has the same (sparse) sparcity pattern as M due to the block structure of M. Thus, the velocities can be eliminated from the approximation double, forming a matrix equation for pressure, with a matrix

$$
B = \mathscr{C}^T M^{-1} C + \frac{1}{\Delta t^2} H = \begin{pmatrix} \mathscr{C}_{\mathrm{g}}^T & \mathscr{C}_{\mathrm{s}}^T \\ 0 & \mathscr{C}_{\mathrm{s}}^T \end{pmatrix} \begin{pmatrix} D_{\mathrm{gg}} & D_{\mathrm{gs}} \\ D_{\mathrm{sg}} & D_{\mathrm{ss}} \end{pmatrix} \begin{pmatrix} C_{\mathrm{g}} & 0 \\ C_{\mathrm{g}} & C_a \end{pmatrix} + \begin{bmatrix} 0 & 0 \\ 0 & \dfrac{1}{\Delta t^2} H_a \end{bmatrix} \tag{38}
$$

This now forms our pressure matrix. An approximation $\hat{B}$ to B that is symmetric/positive definite is formed and is used to precondition the solution of the matrix equations involving B. To this end, suppose $\hat{D}_k = \hat{\underline{\underline{f}}}_k \hat{M}_{kk}^{-1}$ in which $\hat{M}_{kk}^{-1}$ is a further approximation to M_{kk}^{-1}. In this work we use a diagonal approximation obtained by ignoring off-diagonal entries in M_{kk} (see Section 3.2.3 for the motivation of this definition of $\hat{D}_i$). In order to define $\hat{\underline{\underline{f}}}_k$, a diagonal matrix $\underline{\underline{f}}_k$ is first defined with diagonal entries corresponding to a nodewise approximation of the volume fractions α_k (see next section for methods of calculating f_{k_i}). More specifically, $\underline{\underline{f}}_k$ is defined by its entries

$$
f_{k_{ij}} = \delta_{ij} f_{k_i} \quad \text{and} \quad \hat{\underline{\underline{f}}}_k = \begin{pmatrix} \underline{\underline{f}}_k & 0 \\ 0 & \underline{\underline{f}}_k \end{pmatrix} \tag{39}
$$

We have also experimented with lumping M_{ij} via row sum to obtain a diagonal approximation $\hat{D}_k^{-1}$. The off-diagonal entries in M_{ij} are usually negative (because they are dominated by drag forces); this reduces the size of the positive value in the diagonal approximation of M_{kk}. However, simply taking the diagonal entries corresponds to a relaxation scheme and results in a more stable and quickly converging pre-conditioner and overall solution. The diagonal matrix D_k is defined by its coefficients

$$(D_k)_{ij} = f_{k_i}((M_{kk})_{ij}\delta_{ij})^{-1} \quad \text{and so} \quad \hat{D}_k = \begin{pmatrix} D_k & 0 \\ 0 & D_k \end{pmatrix} \quad \text{and} \quad \hat{D} = \begin{pmatrix} \hat{D}_g & 0 \\ 0 & \hat{D}_s \end{pmatrix} \tag{40}$$

The preconditioner for solution of matrix equations involving matrix B thus becomes

$$\hat{B} = \begin{pmatrix} C_g^T & C_g^T \\ 0 & C_g^T \end{pmatrix} \begin{pmatrix} \hat{D}_g & 0 \\ 0 & \hat{D}_g \end{pmatrix} \begin{pmatrix} C_g & 0 \\ C_g & C_g \end{pmatrix} + \begin{bmatrix} 0 & 0 \\ 0 & \dfrac{1}{\Delta t^2} H_a \end{bmatrix} \tag{41}$$

The iterative solution of matrix equations involving matrix B is an Arnoldi iteration [43] in which a number of orthogonal vectors are maintained. The only difference between this and FGMRES [40] is that there is the potential to add any orthogonalized vector in the least squares process, and then to discard when the number of spanning vectors reaches a specified maximum any one of the other spanning vectors. We have experimented with a number of ways of discarding vectors. The best seems to be to discard vectors that have contributed most to the current solution. This is thought to be because when these vectors are discarded other new vectors can be formed that have a similar direction in the search space, which is not the case when these vectors are retained.

The crucial point is that the Arnoldi iteration allows the preconditioning matrix to be different at each iteration, which means that there is no need to solve the matrix equation involving the pre-conditioner to great accuracy—it just needs to be solved to a better accuracy than the current accuracy of the solution in the Arnoldi iteration. Block SSOR preconditioning [43] is used to precondition conjugate gradient iterations. These block matrices are 2×2 because the pressures p_s and p_a are calculated simultaneously. Twenty orthogonal vectors are maintained in the examples presented and these are simply obtained from the Krylov subspace. After 20 iterations the whole process is restarted in much the same way as FGMRES.

It is worth mentioning that instead of using a projection method to solve the coupled discretized momentum and continuity equations, one could again apply Arnoldi iteration to the solution of the pressure equation with the matrix

$$\mathscr{B} = \begin{pmatrix} \mathscr{C}_g^T & \mathscr{C}_s^T \\ 0 & \mathscr{C}_s^T \end{pmatrix} A^{-1} \begin{pmatrix} C_g & 0 \\ C_g & C_g \end{pmatrix} + \begin{bmatrix} 0 & 0 \\ 0 & \dfrac{1}{\Delta t^2} H_a \end{bmatrix}$$

which is obtained by eliminating the velocities from Equation (36) to obtain an equation for pressure. matrix B, Equation (38), above would then be used as a pre-conditioner. To form the matrix vector multiplications involving $\mathscr{B}$, a matrix equation involving A would then need to be solved. In addition, the continuity equation is non-linear so one still needs to iterate around this. However, the projection method approach used here provides a convenient means of doing this (combining linear and non-linear iterations) as the linearized, phase combined, continuity equation (20) is satisfied at the end of each iteration. However, to increase the robustness of the scheme it has been found necessary to introduce a third tolerance; so that only when the discretized continuity and discretized linearized momentum equations have converged to within this tolerance, are the volume fractions updated via Equation (25).

There is a second non-linear solver that is wrapped around the solution method described above. This iterates the non-linear terms in the momentum equations to convergence. When this outer iteration is allowed to convergence, a single inner non-linear iteration can be used, which in effect converges the inner iteration. The minimum requirement is that the non-linear continuity equations (25) are strictly satisfied, and therefore constraints (26) are enforced.

An explicit treatment of the solid-phase pressure can be used in the above formulation so that the pressures $\underline{p}_a$ do not appear in the matrix equation above, then the matrices $\mathscr{C}^T$ and C become

$$\mathscr{C} = (\mathscr{C}_g^T, \mathscr{C}_s^T) \quad \text{and} \quad C = \begin{pmatrix} C_g \\ C_g \end{pmatrix} \quad \text{and} \quad H_a = 0$$

and the pressure vector $\underline{p}$ becomes $\underline{p} = \underline{p}_g$. At the other extreme, all the terms in the solid-phase pressure can be treated implicitly, so the continuity equations (28) are replaced by Equation (23), i.e. H_s replaces H_a in the above. The pressure vector $\underline{p}$ then becomes $\begin{pmatrix} \underline{p}_g \\ \underline{p}_s \end{pmatrix}$.

3.2.3. Second discretization method. To form a second discretization that will be used to help solve the equations above, the volume fraction α_k at each node i, f_{k_i} are first obtained. It can be important to obtain a f_k field that is representative of α_k as this will speed up the convergence of the pressure solver. The values f_{k_i} at each node i can then be employed to obtain a discretization of the term $\nabla \cdot \alpha_k v_k$ and is used to define $\hat{\underline{f}}$ in Equation (39).

Upwind calculated volume fractions $\underline{f}_k$, $\forall i$ combined to form a vector $\underline{f}_k$, that are representative of α_k at the velocity nodes are obtained by solving the equation

$$N_k \underline{f}_k = L_k \underline{\alpha}_k \tag{42}$$

$f_k = \Sigma_j N_j f_{k_j}$ is a continuous function of space whereas α_k need not be continuous. In which case

$$N_{k_{ij}} = \int (N_i + \|J^{-1} v_k\|_\infty^{-1} v_k \cdot \nabla N_i) N_j \, \mathrm{d}V$$

and

$$L_{k_{ij}} = \int (N_i + \|J^{-1}v_k\|_\infty^{-1} v_k \cdot \nabla N_i) M_j \, \mathrm{d}V$$

where J is the Jacobian of the distorted finite element system. In the one-dimensional case

$$\|J^{-1}v_k\|_\infty^{-1} = \frac{h_e}{2|v_k|}$$

in which h_e is the characteristic element length of linear N_i, $\forall i$. The infinity norm is used in the above equation, e.g.

$$\left\| \begin{pmatrix} \alpha_1 \\ \alpha_2 \end{pmatrix} \right\|_\infty = \max(|a_1|, |a_2|)$$

Boundary conditions on the volume fraction fields are applied to Equation (42) to ensure that f_k satisfy these.

Equation (42) ensures that $\int f_k \, \mathrm{d}V = \int \alpha_k \, \mathrm{d}V$ in absence of boundary conditions because the sum of the weighting functions $(N_i + \|J^{-1}v_k\|_\infty^{-1} v_k \cdot \nabla N_i)$ is unity. However, solving Equation (42) for f_{k_i}, $\forall i$ does not ensure that $f_{k_i} \in [0, 1]$, $\forall i$. Note that f_k need not be conserved in order that α_k is conserved in the solution of the continuity equation (18). Thus, f_{k_i} is simply rounded up or down to satisfy $f_{k_i} \in [0, 1]$. This ensures positive-definiteness of the resulting pressure matrix, Equation (41), in the lumped scheme. Solution of Equation (42) does not ensure $\Sigma_k f_{k_i} = 1$ at each node i. This is for the same reason not important. However, a certain limiting case can produce $f_{k_i} = 0$, $\forall k$ (this situation can also occur with the donor cell approach [44]). Thus an additional ad-hoc modification to f_{k_i} is made to ensure $\Sigma_k f_{k_i}$, $\forall i$ reaches a minimum value (e.g. 0.1). This is achieved by adding the deficit into the volume fraction f_{1_i} in which 'l' is the lightest phase.

A discretization of the term $\nabla \cdot \alpha_k v_k$ is $C_g^T \hat{f}_k \underline{v}_k$. The discretized continuity equation then becomes

$$M_\alpha \left(\frac{\alpha_k^{n+1} - \alpha_k^n}{\Delta t} \right) + C_g^T \hat{\underline{f}}_k^{n+1} \underline{v}_k^{n+1} = \underline{0} \tag{43}$$

The resulting α_k is conserved because the sum (integral over the domain) of all the entries in the vector $C_g^T \hat{\underline{f}}_k \underline{v}_k$ is zero. However, α_k can become negative, so this equation is used only to help accelerate the convergence of the linear iteration, i.e. the construction of the pre-conditioner $\hat{B}$ in Equation (41).

3.3. Granular temperature solution

The discretization of the advection terms of the granular temperature equation is the same as for the continuity equation (18). Discretization of the diffusion term in the granular

temperature equation is achieved on a five-point stencil. The resulting discretized temperature equation for T is solved using GMRES with FBGS pre-conditioning and 20 iterations before restarting GMRES.

However, it has been found desirable to introduce a non-linear Pickard iteration over the temperature equation, which allows the non-linear terms in T to be represented more accurately. The resulting temperature T is then used in the discretization of the momentum and continuity equations (36). A maximum of three of these iterations is used. This is one example of 'inner' non-linear iterations used to take the burden off the 'outer' non-linear iterations over the entire time step. This ploy results in a considerably more stable scheme, allowing larger time steps to be used.

3.4. Summary of the solution procedure

In summary, the solution of the multi-phase equations within a time step is as follows:

Outer iteration within a time step:

1. Solve the non-linear granular temperature equations using α_k, $\forall k$; v_k, $\forall k$ and T from the previous iteration or time level (if it is the first iteration of current time level).
2. Using latest temperature and volume fractions calculate the solid-phase pressure p_s and viscosities μ_s and ζ_s.
3. Calculate discretized momentum equations, in Equation (36).
   Non-linear inner iteration:
4. Calculate discretized continuity equations, in Equation (36).
5. Using matrix A of Equation (36), solve Equation (35) for the velocities $\underline{v}_*^{n+1}$, using the pressures $\underline{p}_*^{n+1}$ from the previous iteration, or time level if it is the first iteration.
6. Solve pressure equation (33) for pressure correction.
7. Put pressure correction into pressure and solve the velocity correction equation (34) to obtain the velocity field.
8. Solve the continuity equations (25) for volume fractions.
9. If pressure/velocity/volume fractions have not converged go to (4), else go to (10).
10. If all fields have not converged go to (1) above to obtain improved approximations to non-linear drag, momentum terms, etc., else advance the time level and repeat the whole process.

We have chosen to use Pickard iteration for all non-linear iterations because it has a relatively large radius of convergence, compared with, say, Newton–Raphson-based methods, although some combination of the two methods would perhaps be most efficient.

4. NUMERICAL SIMULATIONS

The numerical modelling described in the previous sections will now be applied to two case studies. In both cases, the gas (air) at room temperature enters from the bottom of the reactor and exits from the top, while the solid-phase (spherical particles) circulates inside the bed.

In this section also, the results of the simulations are compared for cylindrical and Cartesian co-ordinates and the effect of breaking the symmetry, in Cartesian co-ordinates, on the solutions has been investigated.

In order to show the results of the simulations, throughout this work a number of graphs and pictures have been provided. However, to grasp more information about the dynamical behaviour of the fluidized beds studied here, a number of animations are available on the Internet (these can be found at http://amcg.th.ic.ac.uk/multiphase).

4.1. Case study 1: simulation of a fluidized bed reactor in a bubbling regime

The experimental configuration used is described in Reference [45]. It consists of a cylindrical column, 13.8 cm in diameter, that is filled with glass beads with diameters in the range 0.042–0.06 cm. The cylinder is filled to a height of 11.3 cm (static bed height). In the simulations of these experiments, a particle diameter of 0.05 cm and particle density of 2.5 g cm^{-3} have been used. The inlet superficial velocity of air at room temperature is 64.1 cm s^{-1}, 18 per cent of the terminal velocity. A time step of 0.2×10^{-3} s has been adopted for the computations.

A uniformly spaced grid is used in the streamwise direction, while in the cross-streamwise direction an exponential grid is adopted to increase the numerical resolution near the walls.

For this simulation, a 13×20 grid has been used, where the first and second numbers are the number of uniformly spaced elements in the radial (cross-streamwise) and axial directions respectively. The simulation took approximately 1 h of CPU on a Dec Alpha(ev5) 500 in single precision, to reach 10 s.

Based on particle size and density difference between particles and air, the solid-phase can be classified as Geldart B powder, see Reference [3]. For this group of powders, bubbling starts at minimum fluidization [1]. Using the second form of the Thonglimp [46] correlation for gas–solid fluidized beds, the minimum fluidization velocity was calculated to be 19 cm s^{-1}.

The mean velocities over time have been calculated to assess the time averaged behaviour. In the upper parts of the reactor that are seldom visited by particles, the velocity of the solid-phase is that of the free falling particles, which can reach terminal velocity if the reactor is tall enough. This information is of little use to us, and so when the averaged volume fraction is less than 0.05 we have not drawn the averaged velocity vectors in the plot of the solid flow patterns in this fluidized bed (Figure 2(a)). In addition, where the average volume fraction is small (just above 0.05) and in the splash zone, the average velocity will still be dominated by the falling particles, as seen in Figure 2(a). In the main body of the reactor the results of the simulations (Figure 2(a)) show that particles generally ascend at the centre and descend near the wall. This behaviour is consistent with the results of experiments [45] and is shown in Figure 2(b). This comparison suggests that the qualitative behaviour of the simulation agrees well with that of the experiment. The stable height of the bed in the experiment appears to be higher at about 21 cm, see Reference [45] and Figure 2(b), than that of the simulation, which is about 18 cm (Figure 3(a)). Possible reasons for this are: inaccuracy of Ergun's equation (for drag); three-dimensionality of flow; inadequacy of two-fluid model; the experimental coefficients used in the calculations, such as the restitution coefficient of glass beads, the maximum packing factor, the wall restitution coefficient and the friction coefficient of the wall. A restitution coefficient of 0.995 was used in the calculations. While Reference [21] reports that when a
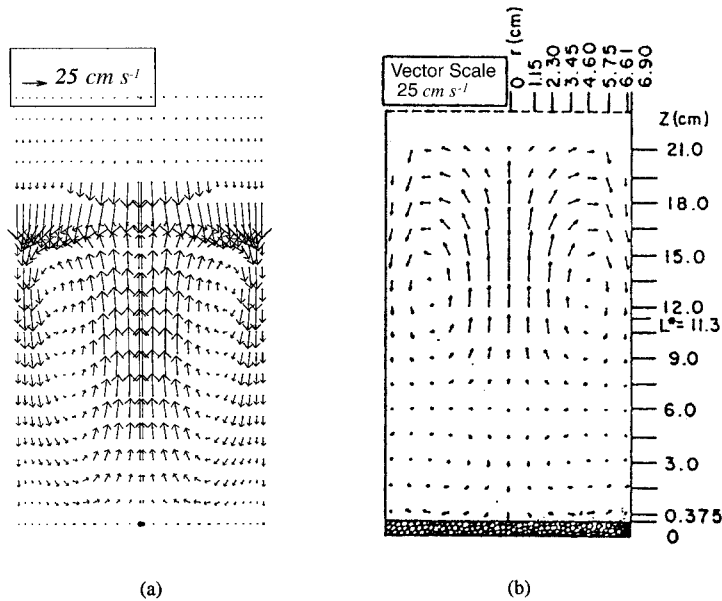
Figure 2. (a) Time-averaged velocity vectors of the particles, calculated by the simulations in the cylindrical co-ordinates. (b) The velocity vectors obtained from experiment (case study 1).

restitution coefficient of 0.995 has been used in their calculations, the results are closer to the experimental results; Reference [47] reports a restitution coefficient of 0.9 for the glass beads. A wall restitution coefficient of 0.75, a friction factor of 0.2 and a maximum packing factor of 0.62 are used for the calculations. Preliminary investigations have shown that the flow is especially sensitive to the friction factor used.

Figure 3 shows the average computed volume fraction of particles, which indicates that, in the time average sense, the particles have higher concentration near the wall than the centre of the bed. The computed average granular temperature of the particles is also shown in Figure 3 and indicates that, in the time average sense, the granular temperature of the bed is higher near the top than the other parts of the bed.

As a result of impulsive initialization, a large pressure gradient is formed at the beginning of the simulation. This forms a large bubble, which moves upwards and is released into the free board of the fluidized bed. After the release of the first large bubble, whose radius is comparable with the diameter of the fluidized bed, new small bubbles form near the bottom of the bed and rise towards the free surface. In general, the bed operates in a bubbling regime.

A variation of void fraction with time at different sample points has been analysed and indicates that the amplitude of the oscillation of the void fractions in the centre of the bed at $z = 5.6$ cm and $z = 11.3$ cm are larger than that at the corresponding heights near the wall, at $r = 5.155$ cm. The results also show a larger amplitude of oscillations at sample points at $z = 11.3$ cm relative to $z = 5.6$ cm, indicating that the voids grow as they approach the surface of the bed.
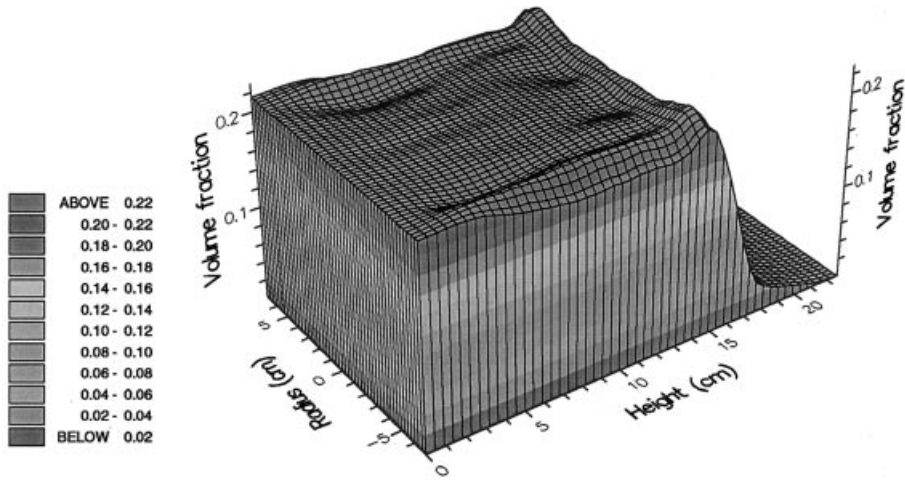
(a) solid volume fraction
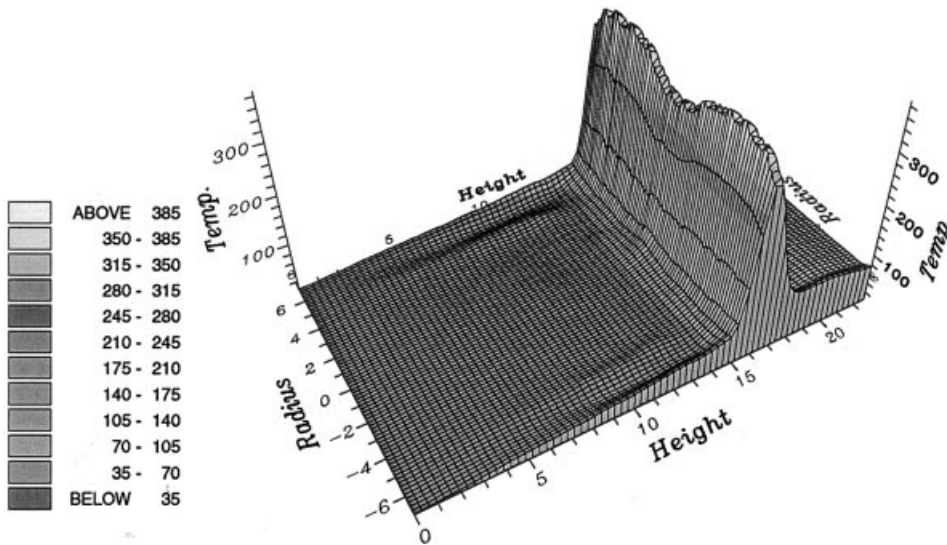
(b) granular temperature

Figure 3. (a) Time-averaged volume fraction of particles. On average, particles have higher concentrations near the walls than near the centre. (b) Time-averaged granular temperature. The granular temperature near the top of the bed is higher than the granular temperature in other regions of the bed (case study 1).

Fourier transform (using a time series consisting of 32 768 points taken from the last 32 768 time steps of the 10-s simulation) has been used to calculate the power spectrum of void fractions at different sample points. A dominant frequency of about 4.3 Hz can be observed

at all the sample points. The frequency of oscillations at the centre and near the wall appears to be the same for the same heights. Comparing the frequencies at different heights indicates that while at $z = 5.6$ cm the only frequencies are at 4.3 Hz and its integer multiples, at $z = 11.3$ cm, beside the frequency of 4.3 Hz, other peaks also coexist.

A fine 40×40 mesh was used to check mesh convergence. This simulation took approximately 10 h of CPU on a Dec Alpha(ev5) 500 in single precision to reach 10 s. The time-averaged results were similar to the coarser mesh results, but the peaks of the power spectrum are shifted to the right. In this case, peaks show a dominant frequency at 5.3 Hz and its integer multiples. This behaviour (shifting the peaks to the right) indicates that as the number of elements increases (or the element size decreases) the variation of void faction is progressively better resolved. The calculated frequencies are consistent with those obtained in the associated experiment [45], in which dominant frequencies in the range of about 3.8–5 Hz were reported. Bubble sizes with diameters of 3 cm were observed frequently in the simulation, which grew as they rose to reach and burst through the free surface. The correlations of bubble size for group B particles of Darton and Werther both predict bubble sizes of the order of 5 cm with a porous distributor plate, see Reference [25]. This discrepancy in simulated and correlated bubble sizes are believed to be due to the fact that the simulated bubbles were toroidal in shape because of the cylindrical co-ordinates used in the simulation, whereas three-dimensional bubbles are roughly spherical.

4.2. Case study 2: simulation of a fluidized bed in a slugging regime

The experimental apparatus operating in the Delft University of Technology [48] has been used to provide data to check the validity of the model. It consists of a 4-m cylindrical column with a diameter of 38.2 cm, while the solid polystyrene particles have a density of 1102 g cm^{-3} and a diameter of 1.899 mm. The gas-phase is air at room temperature with a superficial velocity of 280 cm s^{-1}, 43 per cent of the terminal velocity. The static bed height is 51 cm. A maximum packing factor of 57 per cent is used in the simulations. A finite element mesh consisting of 20×60 elements and a time step of 2×10^{-4} s were employed in the simulations. The elements are uniformly spaced in the x- and y-directions. A 2-m high domain used for the simulation proved to be adequate to minimize the effect of the imposed outlet boundary conditions on the main flow. The simulations with this mesh took approximately 4 h of CPU on a Dec Alpha(ev5) 500 in single precision to reach 15 s. Based on the particle size and density difference between particles and air, the solid-phase can be classified as Geldart D powder [24]. Using the second form of the Thonglip [46] correlation, the minimum fluidization velocity was calculated to be 62 cm s^{-1}, 22 per cent of the gas inlet velocity.

To simulate this problem initially, axisymmetric cylindrical co-ordinates were used. The results showed that due to the highly three-dimensional nature of the problem, two-dimensional cylindrical co-ordinates can not capture all aspects of the flow, and in some cases the results are not correct. For example, they lead to a high concentration of particles at the centre and top of the cylinder (Figure 4(a)), which is not consistent with the results of the experiment [48]. To treat this problem, since a three-dimensional simulation of the flow is very expensive and time-consuming, the simulation was performed in two-dimensional Cartesian $(x-y)$ co-ordinates.

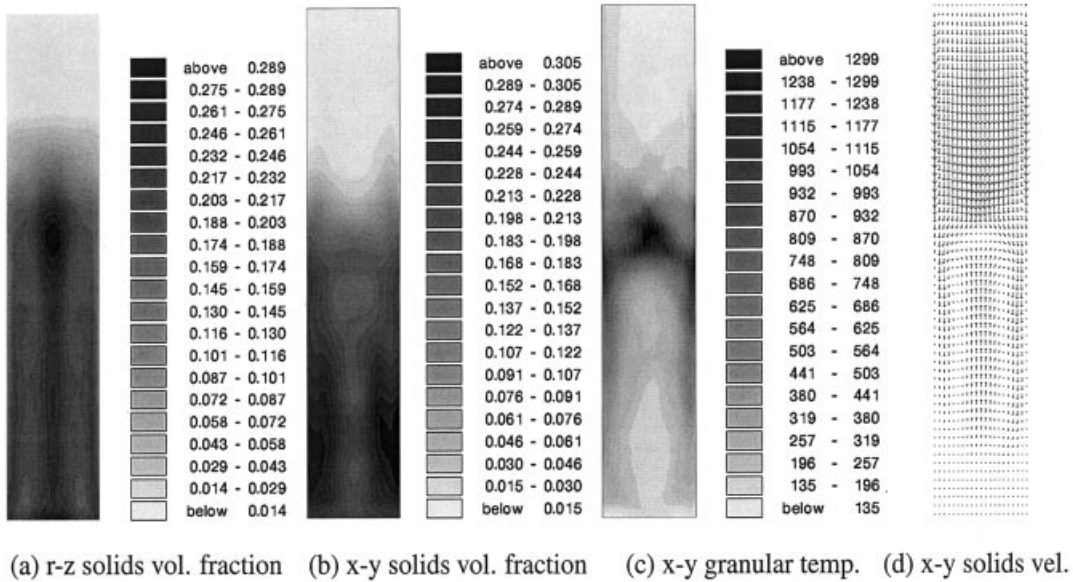(a) r-z solids vol. fraction (b) x-y solids vol. fraction (c) x-y granular temp. (d) x-y solids vel.

Figure 4. Comparison between the time-averaged distribution of volume fraction of particles for (a) axisymmetric cylindrical and (b) Cartesian co-ordinates. Calculations in cylindrical co-ordinates result in a high concentration of particles in the central region of the reactor, while in Cartesian co-ordinates, when the symmetry is broken, a low volume fraction of particles appears in the central region; (c) time-averaged granular temperature of particles; (d) time-averaged velocity vectors of particles. In the time-averaged sense, the particles move upwards near the centre and fall down close to the walls. The magnitude of maximum velocity in this graph is 233 cm s^{-1} (case study 2).

To overcome the problem of having a high concentration of particles in the centre of the bed, symmetry was initially broken by changing the direction of the gravity up to 1 per cent for a short period of time (1 s). Results are time-averaged over 15 s of the simulations. However, as shown in Figure 4(b), the time-averaged results are symmetric (particles fall down near the wall and rise in the central region). This figure shows the time-averaged volume fraction of solid particles inside the reactor and indicates a high voidage in the central region and a high volume fraction of particles near the wall. This behaviour is reported in many experiments. Gajdos *et al.* [49] and Qin *et al.* [50] appear to have been the first to present radial voidage profiles showing high voidage in the centre and much lower voidage close to the wall [3]. The time-averaged granular temperature of particles is shown in Figure 4(c) and indicates a high temperature at the top and near the walls of the reactor. This is due to the higher shear stress in these regions. Figure 4(d) shows the average velocity vectors of the particles and indicates that, in the time average sense, particles move upward at the centre of the bed and fall down near the wall, a phenomena that is consistent with the reported experiment [48] which states that 'bubbles are moving upward in the centre of the zone and particles are falling along the bed wall'. Comparison between experimental results and the simulations shows that
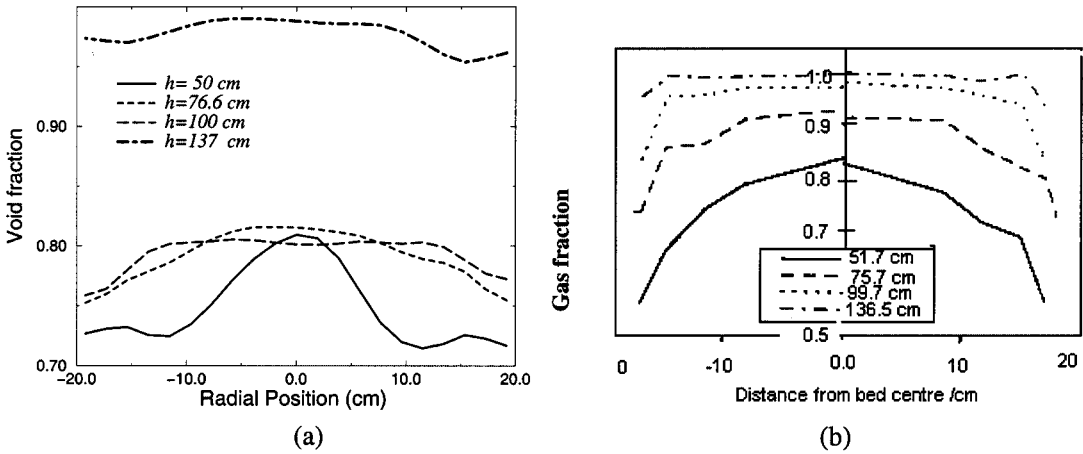
Figure 5. Comparison between results of simulations (a), indicating the distriburion of void fraction at various heightd of the reactor, with that of experiments (b) (case study 2).

while the radial distribution of the void fractions in the simulations are qualitatively close to that of the experiments, axial distributions are different (Figure 5).

Figure 6 shows a time series of volume fraction inside the reactor along with the corresponding auto-power spectra. The large amplitude of the oscillations indicates that the bubbles are
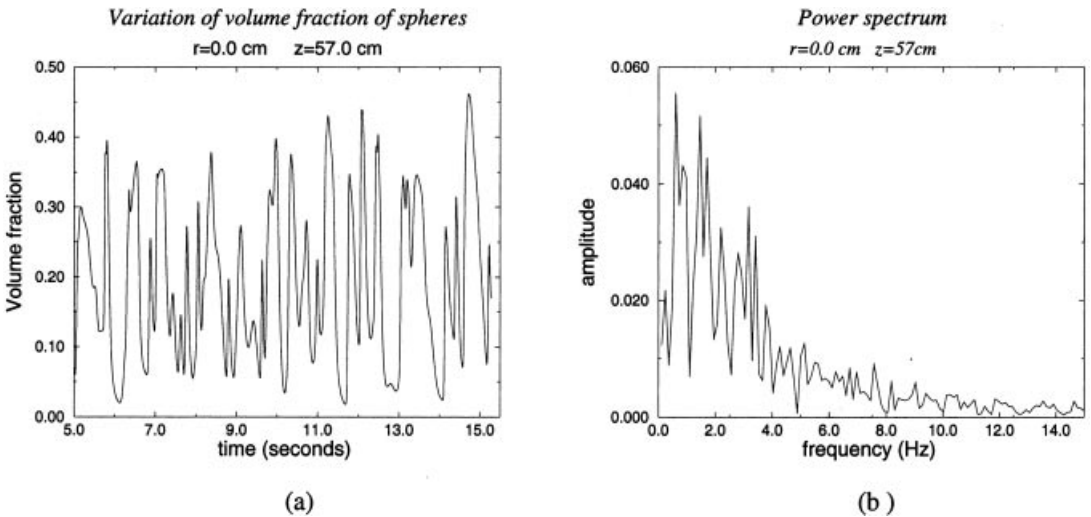

Figure 6. (a) Variation of volume fraction of particles as a function of time; (b) auto-power spectrum of (a) (case study 2—Cartesian co-ordinates).

passing through these positions. To gain some information from these figures, power spectra of the fluctuations of the volume fraction of the particles are calculated, see Figure 6(b) for example. The results at various sample points throughout the bed indicate that different positions of the bed oscillate with different dominant frequencies, ranging from 0.7 to 1.4 Hz. This is consistent with Reference [48] which reports 'The auto power spectral density of gamma signal was calculated in order to study the frequency distribution of gas fraction fluctuations. A dominant frequency band of 1–1.5 Hz appeared in the spectra, both for central and periphery measurements at all axial positions.'

4.2.1. Simulated physics described. Bubbles are subject to elongation when rising along vertical tubes [51] or during interaction. Figure 7(a) and (b) shows the elongation of a bubble along the central axes of the bed. The effect of the walls on changing the direction of motion of the

(a) t=6.1 s   (b) t=6.2 s   (c) t=7.6 s   (d) t=7.7 s

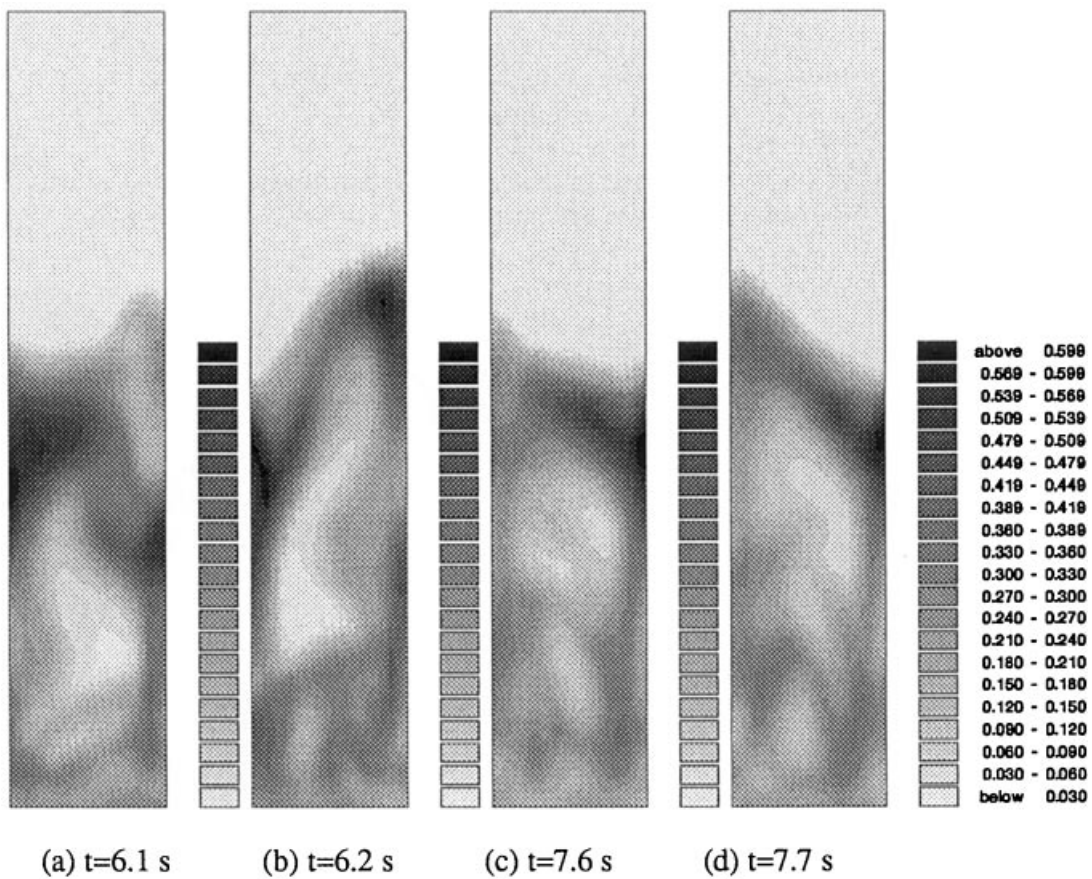|	
above	0.599
0.569 -	0.599
0.539 -	0.569
0.509 -	0.539
0.479 -	0.509
0.449 -	0.479
0.419 -	0.449
0.389 -	0.419
0.360 -	0.389
0.330 -	0.360
0.300 -	0.330
0.270 -	0.300
0.240 -	0.270
0.210 -	0.240
0.180 -	0.210
0.150 -	0.180
0.120 -	0.150
0.090 -	0.120
0.060 -	0.090
0.030 -	0.060
below	0.030

Figure 7. Volume fraction of solid particles at various instances in time showing: (a) and (b) elongation of a bubble; (c) and (d) coalescence as it rises along the central axis of the reactor (case study 2).

bubble is clearly illustrated in this figure. The corresponding velocity vectors of the spherical particles and gas are shown in Figures 8 and 9(a) and (b) respectively. Two counter-rotating vortices behind the large bubble at time $t = 6.2$ s can be observed in the velocity vectors of the particles. The flow of particles in this case is quite similar to flow of a fluid past a bluff body. It can be seen from the velocity vectors of the gas-phase that gas enters from the base of the bubble and exits out of the top.

Coalescence of bubbles has been studied by many workers. Assuming two bubbles centred on a common vertical line rise vertically, Clift and Grace [52] explain that the lower bubble accelerates under the influence of the leader so that coalescence occurs when the lower bubble catches up with the upper bubble. Toei *et al*. [53] explain that for bubbles not in vertical alignment, the lower bubble moves towards the line of rise of the upper bubble, subsequently accelerating vertically to enter its wake, so that coalescence typically occurs with the bubble alignment almost vertical (Figure 7(c) and (d)). However, Cranfield *et al*. [54] explain that
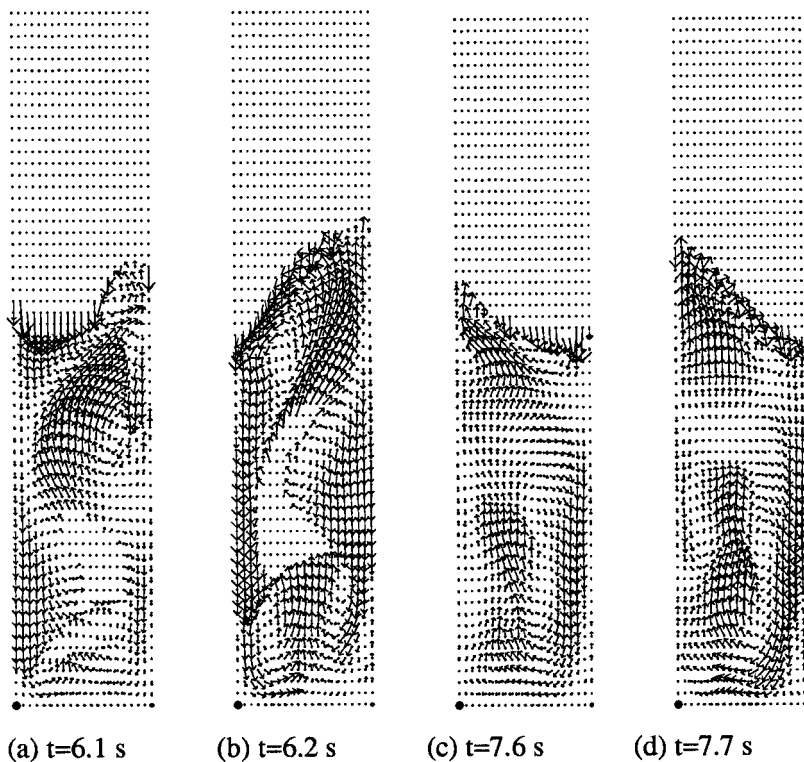

(a) t=6.1 s   (b) t=6.2 s   (c) t=7.6 s   (d) t=7.7 s

Figure 8. Velocity vectors of the particle-phase at different times indicating: (a) maximum velocity = 343 cm s^{-1}; (b) when a bubble elongates—two couter-rotating vortices can be observed below the bubble— maximum velocity = 299 cm s^{-1}; (c) maximum velocity = 386 cm s^{-1}; (d) the bubbles are coalescing— maximum velocity = 312 cm s^{-1} (case study 2).

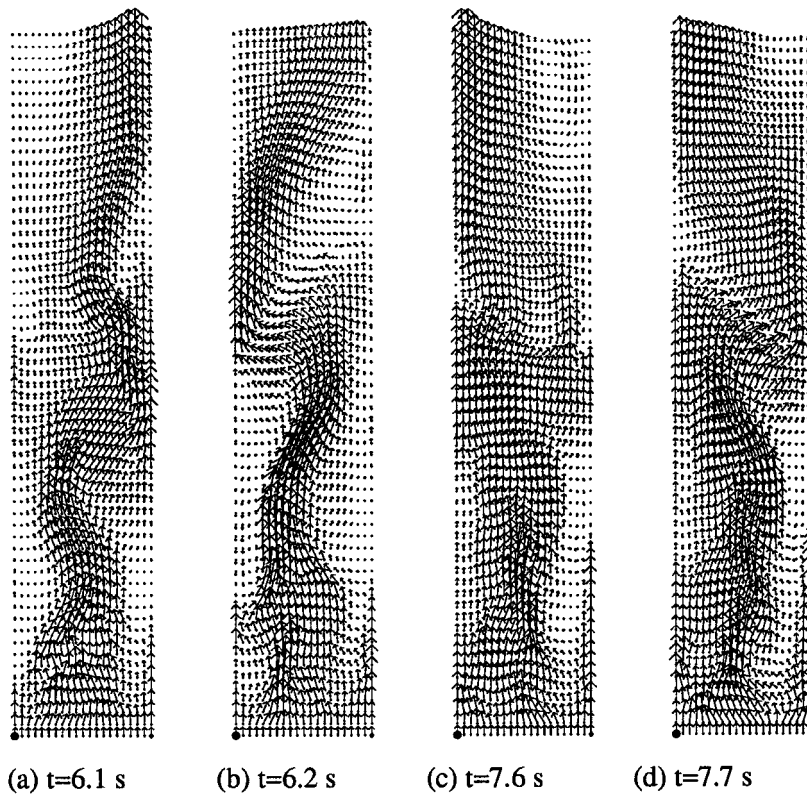(a) t=6.1 s   (b) t=6.2 s   (c) t=7.6 s   (d) t=7.7 s

Figure 9. Velocity vectors of the gas-phase at different times indicating: (a) maximum velocity $= 1130$ cm s^{-1}; (b) when a bubble elongates—maximum velocity $= 1190$ cm s^{-1}; (c) maximum velocity $= 1000$ cm s^{-1}; (d) the bubbles coalescing—maximum velocity $= 930$ cm s^{-1} (case study 2).

'Coalescence in group D beds is much less understood: qualitatively, bubbles appear to grow by absorbing gas from neighbouring bubbles rather than as a result of relative bubble motion.'

Figure 7(c) and (d) shows the process of coalescence of bubbles. A bubble created near the bottom and corner of the bed at about $t = 7.4$ s has moved towards the centre and the line of rise of the upper, by $t = 7.5$ s. At $t = 7.6$ s (Figure 7(c)), the bubble in the centre has entered into the wake of the upper bubble, and at $t = 7.7$ s (Figure 7(d)) the bubbles have coalesced. This is consistent with the explanation of Clift and Grace [52] about coalescence of bubbles. As a result of coalescence of bubbles near the top of the bed, the size of the bubbles near the top are larger than that of those near the bottom of the bed. Since at the top of the bed the size of the bubble is comparable with the diameter of the reactor, this fluidized bed mainly operates in the slugging regime. Figure 8(c) and (d) illustrates the corresponding velocity vectors of the spherical particles. Velocity vectors of the gas-phase are shown in Figure 9(c) and (d). A phenomenon that can be observed in the velocity vectors of the gas-phase is that

the gas flows into the base of the bubble and out of the top, a behaviour that is characteristic of group D of Geldart powders. In this group for large particle systems, all but the largest bubbles travel slower than the interstitial gas and the gas short-circuits the bed by entering the bottom of a bubble and leaving the top [24].

As a bubble approaches the upper free surface of a fluidized bed, a dome is seen to rise in advance of the bubble (Figure 7(b)). A mantle of solids separating the top of the dome from the roof of the bubble thins, until the bubble breaks through [52]. Since relatively large bubbles burst through the bed surface periodically, the bed collapse rapidly and then new bubbles relatively slowly re-expand the bed to collapse again as another bubble bursts through.

5. CONCLUSIONS

A finite element approach to the solution of the two-fluid granular temperature model of gas–solid fluidized beds has been presented. The overall method is efficient and accurate as proven by the simulations of bubbling and slugging gas–solid fluidized beds.

Various phenomena in the two-phase flow, such as formation, coalescence and elongation of bubbles, have been simulated and compared with the qualitative description of behaviour of bubbles presented in the literature.

Imposing two-dimensional Cartesian or cylindrical geometries on the simulated flow often results in poor approximations to the three-dimensional fluidized bed dynamics, as shown in part here. Thus, it seems important to put effort into efficient overall solution methods, the focus of this paper, so that realistic three-dimensional flows can be modelled in future work. Three-dimensional modelling is currently one of our main strands of research, along with the modelling of heat transfer within the bed.

REFERENCES

1. Couderc JP. Incipient fluidization and particulate systems. In *Fluidization* (2nd edn), Davidson JF, Clift R, Harrison D (eds). Academic Press: London, 1985; 1–45.
2. Kuipers JAM, Van Duin KJ, Van Beckum FPH, Van Swaaij WPM. A numerical model of gas-fluidized beds. *Chemical Engineering Science* 1992; **47**: 1913–1924.
3. Lim KS, Zhu JX, Grace JR. Hydrodynamics of gas–solid fluidization. *International Journal of Multiphase Flow* 1995; **21**: 141–193.
4. Jaeger HM, Nagel SR. Physics of the granular state. *Science* 1992; **255**: 1523–1531.
5. Jaeger HM, Nagel SR, Behringer RP. The physics of granular materials. *Physics Today* 1996; **49**: 32–38.
6. Tsuji Y, Kawaguchi T. Discrete particle simulation of two dimensional fluidized bed. *Powder Technology* 1993; **77**: 79–87.
7. Crowe C, Sommerfield M, Tsuji Y. *Multiphase Flow with Droplets and Particles*. CRC Press: Boca Raton, FL, 1988.

8. Hu HH. Direct simulation of flows of solid–liquid mixtures. *International Journal of Multiphase Flow* 1996; **22**: 335–352.

9. de Oliveira CRE. An arbitrary geometry finite element method for multigroup neutron transport with anisotropic scattering. *Progress in Nuclear Energy* 1986; **18**: 227–236.

10. Soo SL. *Fluid Dynamics of Multiphase Systems*. Blaisdell Press: New York, 1967.

11. Gidaspow D, Ettehadieh B. Fluidization in two dimensional beds with a jet. Part II. Hydrodynamic modelling. *Industrial and Engineering Chemistry Fundamentals* 1983; **22**: 193–201.

12. du Plessis P (ed.). *Fluid Transport in Porous Media*. Computational Mechanics Publications: Washington, DC, 1997.

13. Gidaspow D. Hydrodynamics of fluidization and heat transfer: super computer modelling. *Applied Mechanics Review* 1986; **39**: 1–23.

14. Savage SB. Granular flows at high shear rates. In *Theory of Dispersed Multiphase Flow*, Meyer RE (ed.). Academic Press: New York, 1983; 339–352.

15. Shahinpoor M, Ahmadi G. A kinetic theory for the rapid flow of rough identical spherical particles and the evolution of fluctuation. In *Advances in Mechanics and the Flow of Granular Materials*, vol. II, Shahinpoor M (ed.). Trans. Technical Publications: Germany, 1983; 641–667.

16. Lun CKK, Savage SB, Jeffrey DJ, Chepurniy N. Kinetic theories for granular flow: inelastic particles in Couette flow and slightly inelastic particles in a general flow field. *Journal of Fluid Mechanics* 1984; **140**: 223–256.

17. Johnson PC, Jackson. Frictional–collisional constitutive relations for granular materials with application to plane shearing. *Journal of Fluid Mechanics* 1987; **176**: 187–202.

18. Jenkins JT, Savage SB. A theory for the rapid flow of identical, smooth, nearly elastic spherical particles. *Journal of Fluid Mechanics* 1983; **130**: 187–202.

19. Chapman S, Cowling TG. *The Mathematical Theory of Non-uniform Gases*. Cambridge University Press: Cambridge, 1970.

20. Cao J, Ahmadi G. Gas–particle two-phase turbulent flow in a vertical duct. *International Journal of Multiphase Flow* 1995; **21**: 1203–1228.

21. Samuelsberg A, Hjertager BH. An experimental and numerical study of flow patterns in a circulating fluidized bed reactor. *International Journal of Multiphase Flow* 1996; **22**: 575–591.

22. Ding J, Gidaspow D. A bubbling fluidization model using kinetic theory of granular flow. *AIChE Journal* 1990; **36**: 523–538.

23. Lyczkowski RW, Gidaspow D, Solbrid CW. Multi-phase flow-models for nuclear, fossile and biomass energy production. In *Advances in Transport Processes*, Mujumdar AS, Mashelkar RA (eds). Wiley-Eastern: New York, 1982; 198–351.

24. Geldart D (ed.). *Gas Fluidization Technology*. Wiley: Chichester, UK, 1986.

25. Davidson JF, Clift R, Harrison D (eds). *Fluidization* (2nd edn). Academic Press: London, 1985.

26. Spalding DB. Computer simulation of two-phase flows with special reference to nuclear-reactor systems. In *Computational Techniques in Heat and Mass Transfer*, Lewis RW, *et al.* (eds). Pineridge Press: Swansea, 1985; 1–44.

27. Ransom VH, Wagner RJ, Trapp JA. Paper presented at the 3rd CSNI Specialists Meeting on Transient Two-Phase Flow, Pasadena, CA, 1981.

28. Mahaffy JH, Liles DR. Application of implicit numerical methods to problems in two-phase flow. Los Alamos (New Mexico) Report LA-777-NS, vol. I (NUREG/CG-0665) TRAC-PIA, 1979.

29. Bestion D. The physical closure laws in the Cathare code. *Nuclear Engineering Design* 1990; **124**: 229–245.

30. Johnson C. *Numerical Solution of Partial Differential Equations by the Finite Element Method*. Cambridge University Press: Cambridge, 1995.

31. Hui K, Haff PK, Ungar JE. Boundary conditions for high-shear grain flows. *Journal of Fluid Mechanics* 1984; **145**: 223–233.

32. Ma D, Ahmadi G. An equation of state for dense rigid sphere gases. *Journal of Chemistry and Physics* 1986; **84**: 3449–3450.

33. Carnahan NF, Starling KE. Equation of state for nonattracting rigid spheres. *The Journal of Chemical Physics* 1969; **51**: 635–636.

34. Gidaspow D. *Multi-phase flow and Fluidization: Continuum and Kinetic Theory Descriptions*. Academic Press: London, 1994.

35. Schlichting H, Kestin J. *Boundary-Layer Theory* (6th edn). McGraw-Hill: New York, 1968.

36. Jenkins JT. Boundary conditions for rapid granular flow: flat, frictional walls. *Transaction of the ASME* 1992; **59**: 120–127.

37. Gresho PM, Chan ST, Lee RL, Upson CD. A modified finite element method for solving the time-dependent, incompressible Navier–Stokes equations. Part 1: theory. *International Journal for Numerical Methods in Fluids* 1984; **4**: 557–598.

38. Engelman MS, Sani RL, Gresho PM. The implementation of normal and/or tangential boundary conditions in finite element codes for incompressible fluid flow. *International Journal for Numerical Methods in Fluids* 1982; **2**: 225–238.
39. Shinohara K. In *Rheological Property of Particulate Solids*, *Handbook of Powder Science and Technology*, Fayed ME, Otten L (eds). Van Nostrand Reinhold: New York, 1984.
40. Saad Y, Scultz MH. GMRES, a generalised minimum residual algorithm for solving non-symmetric linear systems. *SIAM Journal of Scientific and Statistical Computing* 1986; **7**: 856–869.
41. Jenike AW. A theory of flow of particulate solids in converging and diverging channels based on a conical yield function. *Powder Technology* 1984; **50**: 229–236.
42. Harris SE, Crighton DG. Solitons, solitary waves, and voidage disturbances in gas-fluidized beds. *Journal of Fluid Mechanics* 1994; **266**: 243–276.
43. Golub GH, Van Loan CF. *Matrix Computations*. Johns Hopkins University Press: Baltimore, MD, 1983.
44. Spalding DB. A general purpose program for multi-dimensional one- and two-phase flow. *Journal of Mathematics and Computers in Simulation* 1981; **XXII**: 267–276.
45. Lin JS, Chen MM, Chao BT. A novel radioactive particle tracking facility for measurement of solids motion in gas fluidized beds. *AIChE Journal* 1985; **31**: 465–473.
46. Thonglimp V. Contribution à l'étude hydrodynamique des couches fluidisées par un gaz. Vitesse minimale de fluidisation et expansion, Docteur-Ingenieur thesis, Institut National Polytechnique, Toulouse, 1981.
47. Cody GD, Goldfarb DJ, Storch Jr GV, Norris AN. Particle granular temperature in gas fluidized beds. Fluidization and Fluid Particle System. *AIChE Symposium Series* 1996; **92**: 31–35.
48. Van der Hagen THJJ, van Dam H, Harteveld W, Hoogenboom JW, Khotylev VA, Mudde RF. Studies on the Inhomogeneous Core Density of Fluidized Bed Nuclear Reactor, To be published.
49. Gajdos LJ, Bierl TW. Studies in support of recirculating fluidized bed reactors for the processing of coal. Topical Report on work performed under DOE/EX-C-76-01-2449, Carnegie-Mellon University, Pittsburgh, PA, 1978.
50. Qin S, Liu D. Application of optical fibers to measurement and display of fluidized systems. In *Fluidization 82: Science and Technology*, Kwauk M, Kunii D (eds). Science Press: Beijing, 1982; 258–266.
51. Grace JR, Harrison D. The influence of bubble shape on the rising velocities of large bubbles. *Chemical and Engineering Science* 1967; **22**: 1337–1347.
52. Clift R, Grace JR (eds). *Continuous Bubbling and Slugging*. Academic Press: London, 1985.
53. Toei R, Matsuno R, Tejima T. The coalescence of bubbles in the gas–solid fluidised bed. *Kagaku Kogaku* 1967; **31**: 1238–1239.
54. Cranfield RR, Geldart D. Large particle fluidization. *Chemical and Engineering Science* 1974; **29**: 935–947.
55. Patanker SV, Spalding DB. *Heat and Mass Transfer in Boundary Layers*, 2nd edn., Intertext: London, 1970.